ROYAL SOCIETY
OF CHEMISTRY

PAPER

Check for updates

Characterization of the sedimentation and drying processes of complex mining tailings materials using NMR

SeyedHamed Derakhshandeh, [iD] [a] Jussi Nousiainen,[b] Markus Piekkari,[b]
Joonas Karvo,[b] Aki Auer,[b] Saija Luukkanen,[c] Pertti Sarala, [iD] [c] Ville-Veikko Telkki, [iD] [a]
Elena Kozlovskaya [iD] [c] and Vladimir V. Zhivonitko [iD] *[a]

Sedimentation and drying are important physicochemical processes that play critical roles in the management of mining operations, directly impacting environmental safety and operational efficiency. This study develops a methodology of utilizing portable single-sided nuclear magnetic resonance (NMR) instruments to study free and induced sedimentation as well as drying processes of complex tailings materials from gold mine tailings storage facilities (TSFs) *via* the detection of ^{1}H NMR water signals of the tailings. The results obtained are discussed considering the influence of the physical and mineralogical properties of tailings, such as particle-size distribution, mineral composition, and solid-content percentage. We observed various phases of sedimentation, including short-term and long-term sedimentations, which are characterized by significantly different timescales required for reaching the complete settling of the sludge layers. Moreover, we show that NMR allows the detection of an interesting effect of mechanically induced sedimentation, which is reported only scarcely in the literature. These findings demonstrate the complexity of the sedimentation process and support a clear relationship among the settling rate, particle size, and density of the minerals. In addition, by using a controlled aeration method on top of a single-sided NMR device, we could evaluate the dynamics of the drying process. The utilized NMR methodology is sensitive to slight changes in the water content and mobility *via* the measurements of both the ^{1}H NMR signal amplitudes and the T_2 relaxation times. It allows one to quantify the water content during the transition from slurry-like to sludge-like forms of the studied tailings. The findings can provide valuable tools to characterize tailings sedimentation and dewatering, highlighting the potential of portable NMR as an analytical tool for real-time monitoring and optimization of TSF management strategies.

1. Introduction

Mining operations and mineral processing play critical roles in technological development and the supply of raw materials for various industries.[1] However, mining activities intrinsically generate significant quantities of waste materials referred to as tailings, which pose notable challenges in their management. Tailings are complex slurry-like materials consisting of water, fine mineral particles, and residual chemical reagents that are remaining after mining beneficiation procedures. These waste materials are mainly stored within dynamic structures known as tailings storage facilities (TSFs).[2–5]

Within TSFs, the suspended particles present in the discharged tailings undergo gravitational sedimentation naturally or through further treatments, leading to progressive water separation.[6] This procedure decreases the volume of tailings, improves the structural integrity of tailings storage dams, and enhances the effectiveness of water recovery. Nevertheless, tailings present highly heterogeneous characteristics, with wide variability in particle-size distribution, mineralogical composition, and water-retention ability.[7,8] These inherent properties hinder the accurate prediction of the settling and drying behaviors of tailings, both of which critically influence the mechanical stability and safety of TSFs.[9–11] Therefore, the development and application of innovative analytical approaches to better understand the sedimentation and drying dynamics of these complex materials are essential for improved TSF management and risk mitigation.

Various theoretical and experimental investigations have been conducted to study the sedimentation behavior of tailings

[a] NMR Research Unit, University of Oulu, Oulu, Finland.
  E-mail: vladimir.zhivonitko@oulu.fi
[b] Agnico Eagle Finland Oy, Kittilä Mine, Kiistala, Finland
[c] Oulu Mining School, University of Oulu, Oulu, Finland

materials. Theoretical studies have provided mathematical frameworks for analyzing consolidation and sedimentation phenomena in fine-grained particulate systems, focusing on particle–fluid interactions during settling.[12–16] Experimental approaches, commonly utilizing settling columns instrumented with diverse sensors, have provided valuable insights into how factors such as the initial solid concentration, particle size, and chemical additives (like flocculants) influence the sedimentation process.[17–20] However, these studies generally have limitations, particularly regarding their inability to realize real-time monitoring and to resolve changes within the sediment layers.

Among applied methodologies, nuclear magnetic resonance (NMR) has considerable potential for use in monitoring water mobility within sedimentation systems. NMR is a powerful analytical tool that provides unique insight into the structure and dynamics of molecules in samples. In an NMR experiment, atomic nuclei are subjected to an external magnetic field, followed by perturbation *via* an orthogonal oscillating radiofrequency field. This perturbation excites nuclear spins, and subsequently, a free induction decay (FID) signal is detected. Fourier transformation of the FID signal yields the NMR spectrum in the frequency domain, where the resulting data are sensitive to the local chemical environment of nuclei.[21–23] Low-field NMR instruments have previously been applied by Cabrera *et al.* to investigate the influence of flocculants and coagulants on the sedimentation behavior of oil-sands tailings, differentiating between free and bound water.[24] However, certain capabilities of NMR, such as achieving spatial resolution, capturing depth-specific dynamics, and performing real-time analysis within tailings sediment layers, remain unexplored.

Here, we employ a single-sided NMR instrument, namely the NMR mobile universal surface explorer (NMR-MOUSE) (Fig. 1),[25–28] along with the Carr–Purcell–Meiboom–Gill[29] (CPMG) pulse sequence (Fig. 2), to study the sedimentation and drying processes in tailings derived from a gold mine. We focus on how these processes evolve within the layered structure of the sediment sludge using depth-resolved NMR measurements. This single-sided
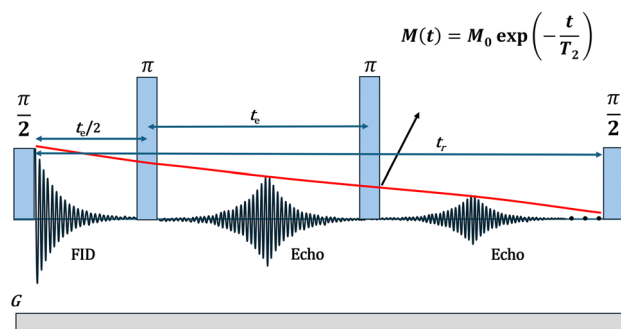

Fig. 2 CPMG NMR pulse sequence diagram, illustrating the signal acquisition and measurement of T_2 relaxation times using NMR-MOUSE during sedimentation and drying experiments. $M(t)$ represents the total magnetization of the sample at the echo maxima at time t after the initial $\pi/2$-pulse. M_0 is the initial magnetization, and T_2 is the transverse relaxation time.

$$M(t) = M_0 \exp\left(-\frac{t}{T_2}\right)$$

portable NMR instrument enables surface and near-surface measurements of transverse relaxation times (T_2) and echo amplitudes, providing a non-destructive means for quantifying the water content and mobility within sediment layers. This versatile device, which is capable of measuring the relaxation and diffusion of samples, has been applied in a wide range of applications, including cultural heritage protection,[25,26,30] food processing,[31,32] breast tissue and mammographic density,[33–35] articular cartilage,[36] cellular exchange processes,[37,38] geopolymerization,[39] and drying.[40–42] Complementary techniques, including particle-size distribution analysis (PSD), mineralogical analysis by X-ray diffraction (XRD), and energy dispersive spectroscopy (EDS) analysis, in conjunction with scanning electron microscopy (SEM) to determine the elemental composition of a sample, were integrated to relate our NMR findings to the physical and mineralogical properties of the samples. In general, the proposed approach can provide a detailed understanding of moisture dynamics, structural evolution, and the influence of mechanical disturbances (such as shaking and drying). Our findings demonstrate the strong potential of single-sided NMR instruments for real-time monitoring of tailings behavior, emphasizing the role of the particle-size distribution and mineral composition in sedimentation and dewatering efficiency.
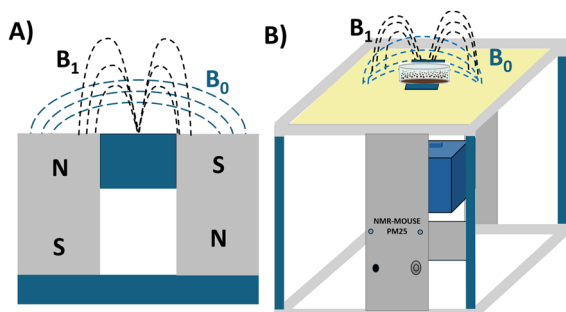

Fig. 1 (A) Schematic of NMR-MOUSE PM25 used in this study. The device features a permanent magnet in conjunction with a surface RF coil to generate static B_0 and oscillating B_1 magnetic fields, respectively, enabling localized, non-invasive ¹H NMR measurements of water content in near-surface regions.[25–28] (B) NMR-MOUSE PM25 device mounted on a lift for vertical sample profiling of a tailings sample.

2. Experimental section

2.1. Samples and their preparation

All samples used in this study were collected from the carbon-in-leach (CIL) tailings storage facility (TSF) associated with a gold mining and beneficiation operation located in the Lapland region of Finland. Tailings are deposited using the beach deposition method in this TSF, which promotes a gradual settling of solid particles as the material is discharged radially across the storage area. Six sampling points were selected along the TSF borders, each located approximately 22 meters apart from the marginal zone of the TSF. Samples were collected from settled tailings formed by tailings discharge across the TSF surface. Additionally, a water sample was sourced from the

reclaim pond within the same facility to serve as the liquid phase in the preparation of slurry samples.

Using these raw materials, six distinct slurry samples designated S1 through S6 were prepared. Each sample consisted of a certain mass of the sampled moist sediments combined with a measured volume of the reclaim pond water. Sample S1 was composed of 17.25 g of raw sediment mixed with 36 mL of reclaimed water. Samples S2 through S6 were each prepared by mixing 16.25 g of raw sediments with 25 mL of reclaim water. Due to the natural variability in the moisture content of the sediments from different locations, the resulting slurries had different solid content values. The solid contents of the samples were S1: 26.4%, S2: 29.5%, S3: 25.2%, S4: 26.1%, S5: 27.9%, and S6: 28.8%. The variation in the solid contents reflects the heterogeneity of the tailings materials around the TSF and is expected to influence the subsequent sedimentation and drying behavior observed during NMR experiments.

We note that the solid content refers to the mass of solid as a percentage of the total mass of the slurry. To determine the initial water content of each sampled sediment, a known mass of wet sediment was oven-dried at 250 °C for 4 hours, and the moisture content was calculated based on the difference between the wet and dry masses. This value was subsequently used to compute the solid content of each slurry sample. The detailed procedures regarding the solid-content percentage calculations are provided in the SI (Section S1.2).

2.2. NMR measurements

NMR measurements were carried out using an NMR-MOUSE PM25 device with the Kea2 console (Magritek, Aachen, Germany) operated *via* the Prospa software. This device is a single-sided, low-field mobile NMR device built using two permanent magnets with opposite pole directions to generate the static B_0 polarization field and a surface coil located between the magnets to provide the B_1 RF field (Fig. 1A). The entire setup is mounted on an adjustable lift, facilitating the vertical profiling of the sample (Fig. 1B). The instrument operates at a 13 MHz ^{1}H NMR resonance frequency and has a virtually constant magnetic field gradient of 7.28 T m^{-1} in the sensitive region, providing a spatial resolution of less than 100 μm, with a maximum measurement depth of 25 mm in profiling experiments. Depth measurements are possible by varying the distance between the B_0 magnet and the sample surface.

In our experiments, NMR-MOUSE was used to measure the T_2 relaxation times and signal amplitudes within the sediment layer as sedimentation and drying progressed. These parameters are indicative of the water content and mobility within the sediment matrix. The CPMG pulse sequence (Fig. 2) was applied for all NMR experiments. The echo time (t_e) was set to 200 μs; 250 echoes were collected, and a repetition time (t_r) of 1000 ms was used. Both the 90° and 180° pulse lengths were 5.5 μs, and 64 scans were averaged to improve the signal-to-noise ratio. All measurements were performed using cylindrical plastic containers with a diameter of 53 mm and a height of 28 mm.

For all sedimentation experiments, the sensitive region in the samples was a layer of *ca.* 100 μm in thickness. The region
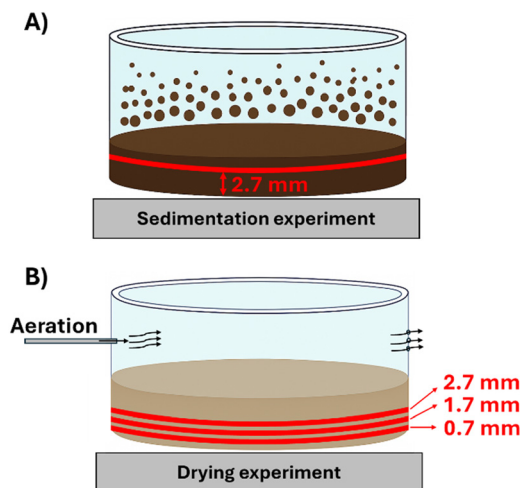

Fig. 3 Sensitive layer positions in the NMR experiments. (A) In the sedimentation experiments, the sensitive layer was fixed at 2.7 mm from the bottom of the container. (B) In the drying experiments, the depth-resolved measurements were taken at 0.7, 1.7, and 2.7 mm to capture vertical moisture gradients.

was positioned at 2.7 mm above the bottom of the sample container (see Fig. 3A) to perform measurements within the sedimented sludge layer. For drying experiments, the measurements were conducted at three distances (0.7, 1.7 and 2.7 mm) from the bottom of the containers, corresponding to different depths within the sediment layer. This approach enabled depth-specific monitoring of moisture distribution during desiccation (Fig. 3B).

2.3. Experimental protocols

2.3.1. Short-term sedimentation experiment. In the short-term sedimentation study, each slurry sample was initially subjected to thorough agitation to ensure homogeneous distribution of solids in the liquid. Immediately following the mixing, samples were positioned on the NMR device for continuous monitoring, taking over a period of two hours. During this time, CPMG measurements were performed repeatedly to track dynamic changes in the water content and mobility associated with the rapid formation of a sediment layer shortly after agitation.

2.3.2. Long-term sedimentation experiment. To further evaluate the behavior of the sample over an extended period, long-term sedimentation experiments were conducted. Following the completion of the short-term study, the sample after the short-term sedimentation experiment remained undisturbed on top of the NMR magnet for an extended observation period of three weeks. Regular CPMG measurements were conducted throughout this period to capture the changes in water dynamics and any progressive compaction occurring within the sediment layer as a function of the prolonged settling time.

2.3.3. Induced sedimentation experiment. This experiment aimed to explore the influence of mild mechanical agitation on water redistribution within the formed layer of the sediment. For this purpose, after short-term or long-term sedimentation experiments, the samples were subjected to gentle mechanical

shaking events designed to avoid significant disruption of the sediment structure. The shaking procedure was performed gently by hand, avoiding mixing the sediment layer settled after the short-term sedimentation experiments with the supernatant water on top of it. Each shaking event lasted for 1 minute, followed by CPMG measurements over a total observation period of two hours. The recorded variations in the T_2 relaxation and signal amplitude were analyzed to assess the impact of induced motion on the fluid migration within the sediment matrix. Once both parameters stopped changing, indicating that no further compaction and water-content alterations occurred within the sediment layer, the shaking procedure was stopped.

2.3.4. Drying experiment. Upon completion of all sedimentation-related experiments, the supernatant water above the sediment was carefully removed. The remaining sediment layer was subsequently placed on the NMR-MOUSE and continuously exposed to a controlled flow of compressed air at a rate of 1 cubic foot per hour (*ca.* 472 cm^3 min^{-1}) (Fig. 3B). Throughout the drying process, CPMG experiments were performed at regular intervals to characterize changes in the moisture content and water mobility. In addition, the spatial profiling capability of the NMR-MOUSE was utilized to perform depth-resolved measurements in three vertical positions (Fig. 3B), thereby enabling real-time monitoring of the water content at different sediment depths during the drying phase.

2.4. Complementary analyses

To assess the influence of mineralogical composition and particle-size characteristics on the observed sedimentation and drying behaviors, additional analytical techniques were applied.

2.4.1. Particle-size distribution (PSD). Particle-size analysis was performed using a Beckman Coulter LS13320 laser diffraction particle-size analyzer to characterize the grain-size profile of the sediment samples. The resulting data indicated a broad distribution of mean particle sizes, with minimum and maximum values ranging from 8.95 µm in sample S1 to 30.98 µm in sample S6 (Fig. 4). Detailed information about the PSD results is provided in SI (Section S2.2).

2.4.2. Mineralogical composition. The mineral content of the samples was characterized using a Rigaku SmartLab 9 kW X-ray diffraction (XRD) system. XRD analysis revealed variations in the abundance of key minerals, including muscovite (mica), gypsum, feldspars (albite and anorthite), quartz, hydronium jarosite, and minor oxides (such as rutile). These results highlight the diverse mineralogical profile with varying density distributions across samples (Fig. 5), reflecting the heterogeneous nature of the tailings collected from six locations around the TSF. This heterogeneity is likely to influence the sedimentation kinetics by affecting the settling velocity of individual mineral particles. Complete diffractograms and peak assignments are included in SI (Section S2.3).

2.4.3. Microstructural and elemental analysis. High-resolution imaging and elemental analysis of the sediment samples were conducted using a Zeiss Sigma field-emission scanning electron microscope (FESEM), equipped with energy-dispersive X-ray spectroscopy (EDS). This technique was employed to complement the particle size and mineralogical
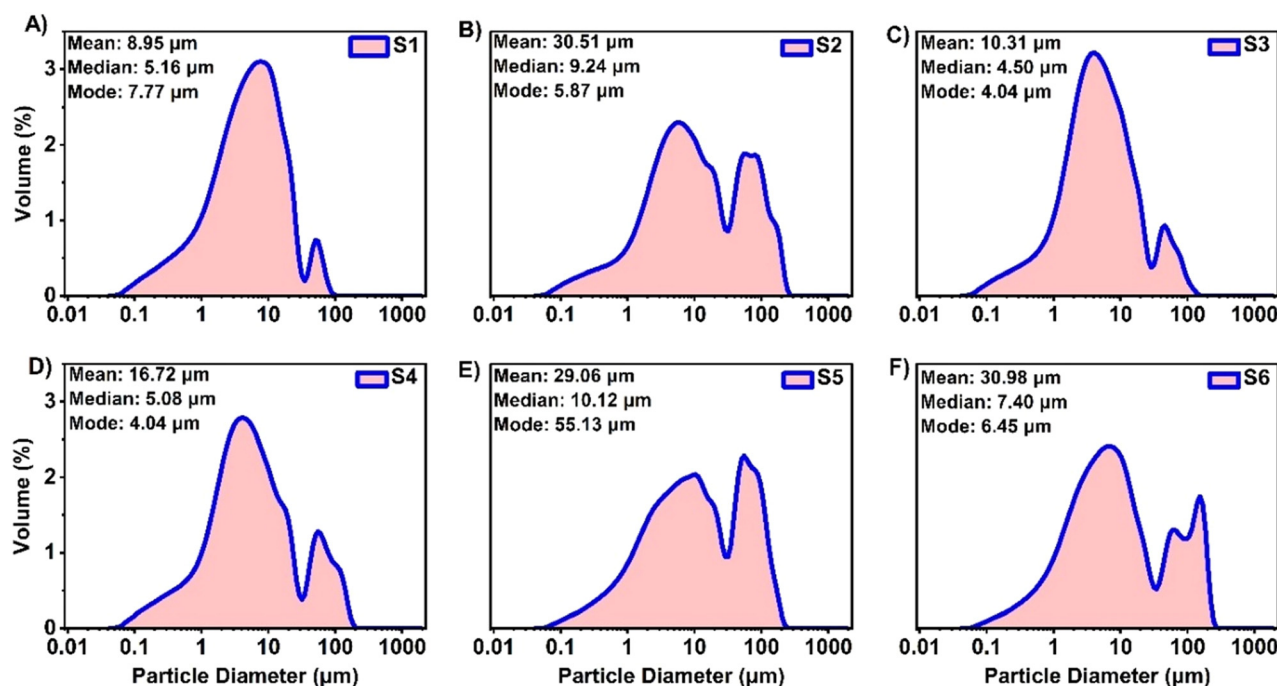

Fig. 4 Particle-size distribution (PSD) graphs for samples S1 to S6 (A)–(F), respectively, illustrating a broad range of particle diameters with specific mean, median, and mode values for each sample. These distributions highlight the variability in particle size across different locations within the tailings storage facility.
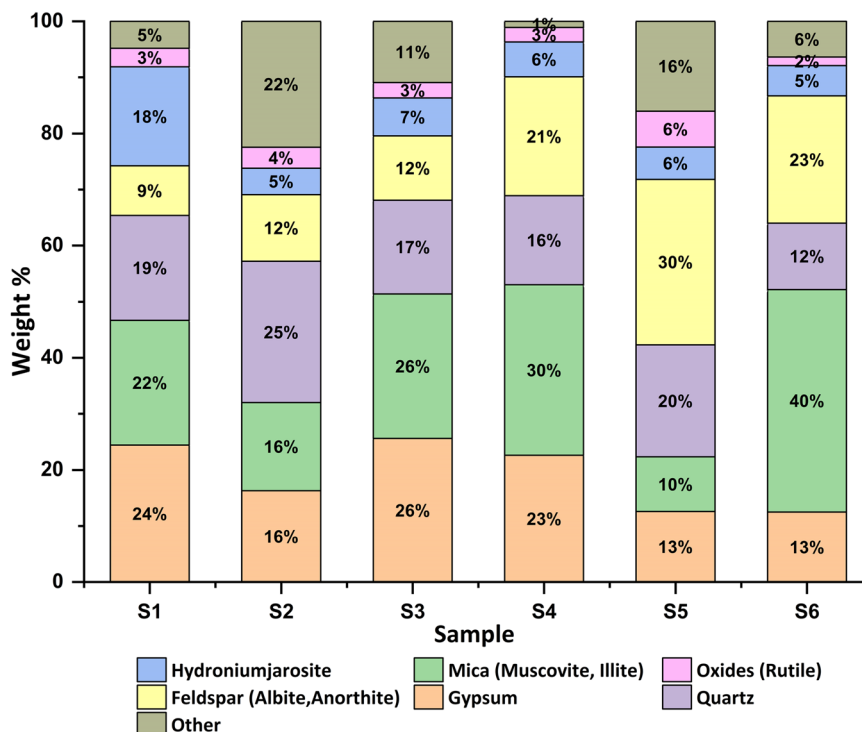
Fig. 5 Distribution of minerals in CIL tailings samples S1–S6 according to XRD analysis. The chart highlights the mineralogical diversity and density variations across different sediment samples, emphasizing the heterogeneous nature of the tailings.

data by providing direct visualization of individual particles and their surface characteristics. The analysis revealed (Fig. 6) that mica (muscovite) and gypsum tended to occur as relatively large particles, while albite, rutile, and quartz were typically of intermediate sizes. Notably, hydronium jarosite consistently appeared as the finest-grained phase. Representative images and full elemental compositions are available in SI (Section S2.4).

3. Theoretical background

3.1. Sedimentation dynamics and Stokes' law

When a single spherical particle falls into a fluid under a laminar condition, the settling rate of the particle is governed by the forces exerted on it. Initially, the particle experiences acceleration due to the gravitational force F_g, which acts downward. However, this force is countered by buoyancy F_b and drag F_d forces exerted by the fluid to retard the particle[43–46] (Fig. 7).

The force balance leads to a constant terminal velocity if

$$F_g = F_b + F_d. \tag{1}$$

The gravitational force F_g and the buoyancy force F_b in eqn (1) can be formulated as

$$F_g = \rho_s \frac{\pi d^3}{6} g \tag{2}$$

and

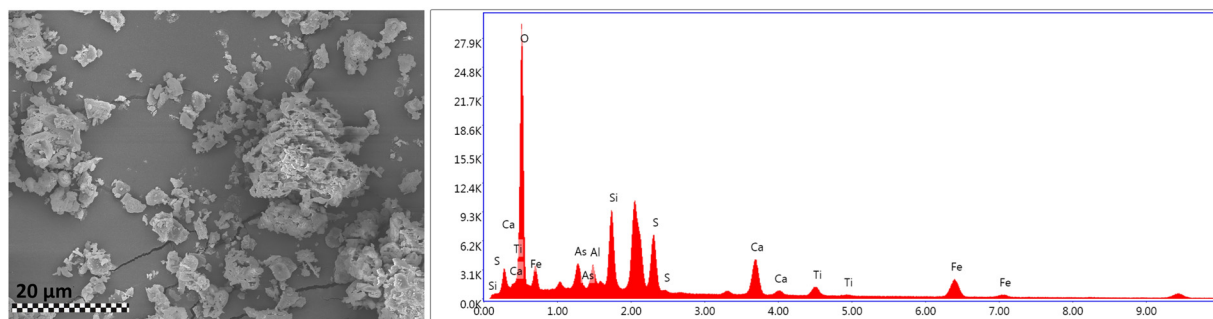$$F_b = \rho_f \frac{\pi d^3}{6} g, \tag{3}$$

Fig. 6 FESEM image (left) and EDS spectrum (right) of sample S1, showing particles with elemental composition dominated by silicates, sulphates, and oxides.
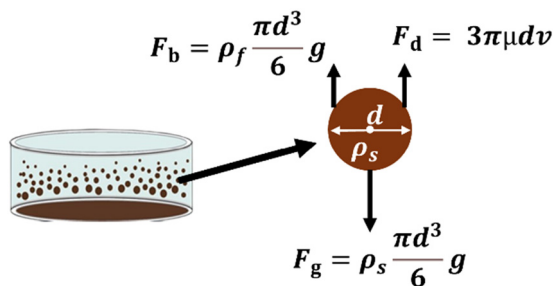
Fig. 7 Forces acting on a spherical particle, including fluid gravitational F_g, buoyancy F_b, and drag F_d forces. Together, they determine the particles' settling velocity under laminar flow conditions.

where ρ_s is the volumetric mass density of the settling particle, ρ_f is the volumetric mass density of the fluid, d is the diameter of the particle, and g is the acceleration due to gravity.

The drag force can be described as

$$F_d = \frac{1}{2} C_D A \rho_f v^2, \tag{4}$$

where C_D is the drag coefficient, A is the cross-sectional area of a particle, and v is the speed of the particle relative to the fluid.

The Reynolds number (Re_p) for a particle with a diameter d falling through a fluid medium with a dynamic viscosity μ at a speed of v is

$$\mathrm{Re}_p = \frac{\rho_f v d}{\mu}. \tag{5}$$

This number is a dimensionless number that describes the nature of the flow around a spherical object.

The drag coefficient C_D in a laminar regime $\mathrm{Re}_p < 1$ is defined as

$$C_D = \frac{24}{\mathrm{Re}_p}. \tag{6}$$

Assuming laminar conditions and combining eqn (4)–(6), the drag force F_d based on the Navier–Stokes equations can be described as

$$F_d = 3\pi\mu d v. \tag{7}$$

Combining eqn (1)–(3), and (7) gives the terminal velocity (the Stokes settling velocity) of a spherical particle in a fluid

$$V_t = \frac{(\rho_s - \rho_f)d^2 g}{18\mu}. \tag{8}$$

We note that eqn (8) describes the terminal velocity of a single spherical particle moving under laminar flow conditions. However, tailings samples are a mixture of different minerals with diverse particle sizes and different shapes. Their motions are affected by interparticle interactions, flocculation, hindered settling, and variations in effective viscosities.[47–51] At the same time, the Stokes' law can provide valuable theoretical estimates of the sedimentation times, highlighting the effects of particle sizes and densities on the sedimentation rates of tailings samples.

For example, Fig. 8 shows the expected ranges of settling times calculated using eqn (8), taking into account the
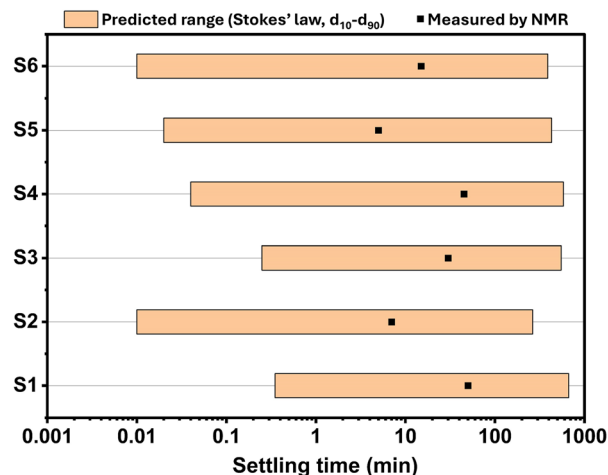

Fig. 8 Estimated settling times for samples S1–S6. Orange horizontal bars represent the theoretical settling time ranges calculated using Stokes' law and d_{10}–d_{90} particle sizes from the size distributions in Fig. 4. The lower and upper settling time limits correspond to the settling times calculated for the d_{90} particle sizes of the most dense mineral phase in each sample. The upper settling time limits correspond to the settling times calculated for the d_{10} particle sizes of the least dense mineral phase in each sample. Squared black points represent the experimentally observed settling times in short-term sedimentation NMR experiments.

experimental geometry in Fig. 3, particle-size distributions in Fig. 4, and mineralogical profiles in Fig. 5 (see SI for details, Section S2.5). This graph indicates a very broad range of settling times for two representative particle sizes, d_{10} and d_{90}, from the size distributions for samples S1–S6. Notably, the experimentally measured settling times during the short-term sedimentation NMR experiments (black points in Fig. 8) fall closer to the middle (*i.e.* d_{50}) of the expectation ranges. This analysis supports a semi-qualitative comparison of the sedimentation properties of our samples in Section 4.4 using mean particle sizes. We note that if the particle-size distributions of individual minerals in the samples, *i.e.*, mineral-by-mineral size distributions, were known, the expectation ranges in Fig. 8 could be made narrower.

3.2. NMR measurement, signal intensity, and T_2 relaxation time

The CPMG pulse sequence is a widely used tool in various applications of single-sided NMR. It is an efficient tool for measuring transverse relaxation times (T_2), which can be extracted from the CPMG multi-spin-echo train that decays over the measurement time due to the transverse nuclear spin relaxation (Fig. 2). The initial spin-echo signal amplitude in a CPMG experiment reflects the proton density that is proportional to the water content. The transverse magnetization associated with a spin-echo signal detected at time t is given by[21,28,52]

$$M(t) = M_0 \exp\left(-\frac{t}{T_2}\right), \tag{9}$$

where M_0 is the initial transverse magnetization.

In practice, especially in single-sided NMR, magnetic field inhomogeneities lead to additional dephasing; thus, the observed decay reflects an effective relaxation time ($T_{2\text{eff}}$),[28,53,54] which is referred to as T_2 in this study for simplicity. Generally, the observed T_2 relaxation times of a fluid in a porous environment, like the tailings slurries, are characterized by three factors:[55,56] bulk fluid relaxation, surface relaxation, and signal decay caused by the diffusion of molecules in the strong magnetic field gradient of the single-sided NMR instrument (7.28 T m^{-1} for our NMR-MOUSE instrument) as well in the internal magnetic field gradients intrinsically present in the heterogeneous samples:

$$\frac{1}{T_2} = \frac{1}{T_{2\,\text{bulk}}} + \frac{1}{T_{2\,\text{surface}}} + \frac{1}{T_{2\,\text{diffusion}}}$$
$$= \frac{1}{T_{2\,\text{bulk}}} + \rho_s \frac{S}{V} + \frac{1}{12} D(\gamma G t_e)^2. \quad (10)$$

Here, ρ_s is the surface relaxivity reflecting the ability of pore walls to induce relaxation, S/V is the surface-to-volume ratio of the porous space, D is the molecular diffusion coefficient, G is the magnetic field gradient strength, γ is the gyromagnetic ratio, and t_e is the echo time.

In porous media, such as sedimented tailings materials containing paramagnetic minerals studied in the presence of a strong magnetic field gradient, the effective T_2 relaxation time is dominated by the contributions of $T_{2\,\text{surface}} = \rho_s S/V$ and $T_{2\,\text{diffusion}} = D(\gamma G t_e)^2/12$, whereas the term including $T_{2\,\text{bulk}}$ can be neglected. Our estimations based on variable echo-time experiments for selected tailings samples indicate the dominance of the internal magnetic field gradient $T_{2\,\text{diffusion}}$ contribution to the apparent T_2 decays (see SI, Section S2.6). The comparison to bulk water diffusion at short diffusion times shows that, on average, water molecules experience 3–3.5 times stronger magnetic field gradients in the heterogeneous matrix of tailings sediments than the constant gradient produced by the NMR-MOUSE instrument. This observation implies a strong influence of internal magnetic field gradients originating from the pronounced magnetic susceptibility differences between water and diverse solid mineral particles in the porous matrix. According to our analysis, this effect on average generates internal gradients of 14–18 T m^{-1} in our magnetic field (0.3 T). These values, for instance, roughly match the reported estimations of internal gradients in Fe(III)-doped kaolin clays, which were shown to be up to 10 T m^{-1} inside pores and exceed 1000 T m^{-1} at the pore surface for a 0.8 T magnetic field.[57] Our samples contain significant amounts of hydronium jarosite, which is the Fe(III) mineral (Fig. 5). Naturally, the surface relaxation contribution, $T_{2\,\text{surface}}$, is also present, but its influence seems to be less pronounced.

To extract the effective T_2 values from the decaying train of echo amplitudes generated in the CPMG pulse sequence, the measured signals were typically fitted using a mono-exponential decay model (Fig. 9A). At the same time, we note that in many cases, the bi-exponential decay model provided a slightly better fit to the sedimentation data, reflecting the real physical heterogeneity within the sample, which can be

attributed to the formation of different pore cavities in the samples. This observation was clearly evidenced in the relaxation time distributions obtained from the CPMG data using a Laplace inversion procedure in the Prospa software of NMR-MOUSE. It typically revealed a dominant fast-relaxing component and a much smaller slow-relaxing component. For example, the distribution for sample S1 showed two peaks (Fig. 9B) at 5.2 and 11.4 ms, consistent with the presence of both fast and slow-relaxing water environments. However, given that the primary objective of this study is to track the overall progress in the sedimentation process over time, the mono-exponential model was selected for the final analysis. This simpler approach showed high sensitivity to capture average relaxation behavior for real-time continuous monitoring of the sedimentation process with a good signal-to-noise ratio. In the case of bi-exponential fitting, the analysis of the individual components produced unwanted numerical noise. Moreover, comparative evaluation showed that the T_2 values obtained from mono-exponential fitting closely matched the average weighted
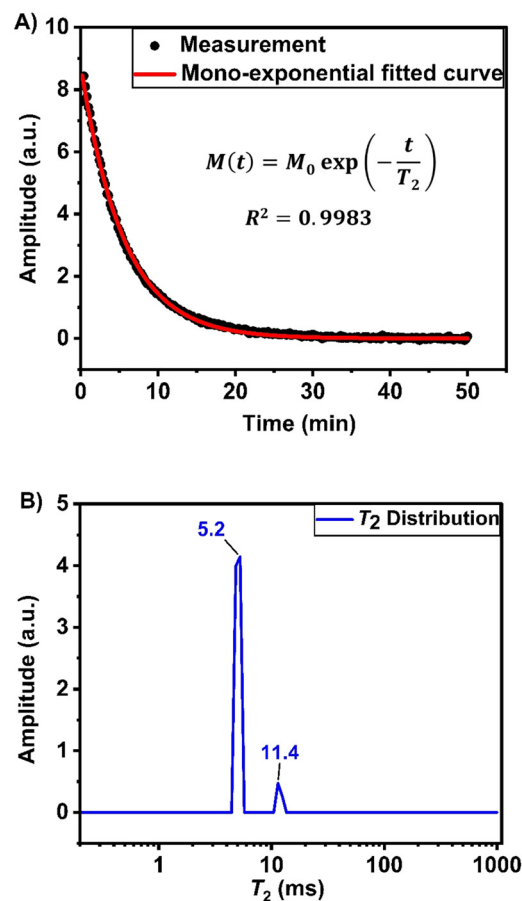

Fig. 9 (A) T_2 decay curve measured in a typical CPMG experiment with sample S1, along with its mono-exponential fit. The close agreement between the measured data (black dots) and the fitted curve (red line) demonstrates the suitability of the mono-exponential model. (B) Relaxation time distribution obtained using the Laplace inversion procedure, showing two distinct components at 5.2 ms (dominant) and 11.4 ms (minor).

T_2 values calculated from the bi-exponential model (see SI, Section S1.3).

We note that since in this work we focus on the sedimentation and drying dynamics as studied by NMR, further detailed investigation of individual T_2 components of tailings sludges lies outside the scope of this manuscript and will be addressed in a dedicated separate study in the future.

4. Results and discussion

4.1. Short-term sedimentation (sample S1)

The short-term sedimentation is characterized by initial rapid free settlement of the tailings sludge layers after rigorous shaking of tailings samples (Fig. 10). Both signal amplitude and transverse relaxation time (T_2) were continuously monitored to track variations in the water content and mobility over time in the bottom layer of the sample containers (Fig. 3A).

All investigated samples demonstrated significant changes in both spin-echo signal amplitude and T_2 relaxation time obtained from the CPMG experiments. Representative examples of the measured data are shown for sample S1 in Fig. 11A (spin-echo amplitude) and Fig. 11D (T_2 time derived from a mono-exponential fitting model). Over the two-hour experimental timeframe, a progressive decrease in the signal amplitude from approximately 8.4 to nearly 7.1 arbitrary units (a.u.) was observed in the former case, while a substantial reduction in T_2 relaxation time from approximately 5.5 to 2.3 ms was observed in the latter case. Notably, the most significant changes in these parameters were visible during the initial 50 min of the experiment, indicating a rapid phase of the sediment layer compaction that occurs shortly after mixing.

These findings suggest that the early stages of sedimentation are dominated by initial rapid settling processes that markedly influence the water distribution and mobility within the system. The short-term sedimentation repeatability was evaluated using multiple replicates of sample S1. For detailed results and repeat analysis spectra, see SI (Section S2.1).

Additionally, visual observations confirmed the formation of a distinct sediment layer and a clear supernatant water phase on top within the first 50 minutes of the experiment, as illustrated in Fig. 10. This visibly distinct phase separation qualitatively confirms the sediment-layer formation detected by the NMR measurements.
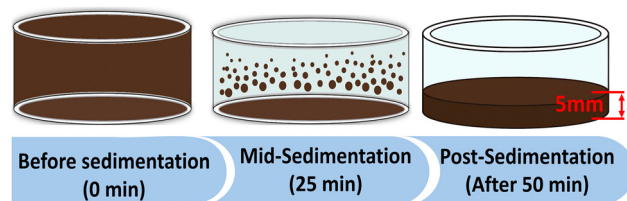

Fig. 10 Sedimentation stages qualitatively illustrating the state of the samples at 0, 25, and 50 min after a rigorous shake, highlighting the initial formation of a sediment layer and the increasing clarity of the supernatant. The timeline matches the observations for sample S1 during the short-term sedimentation and was approximately similar for almost all samples.

The monitoring of the short-term sedimentation using NMR provided real-time information about both the settling and structural changes of the slurry. The significant reduction in the signal amplitude observed during the first 50 min reflects the decrease in the water content within the forming sediment layer, attributed to particle settling and progressive compaction. As the sediment layer forms, part of the water is replaced by the sedimented particles, leading to the observed decrease in signal amplitudes. Simultaneously, the reduction in T_2 relaxation time reflects increasingly confined water environments and reduced molecular mobility, corresponding to greater sediment density and progressive structural compaction within the layer.

4.2. Long-term sedimentation (sample S1)

Continuous monitoring of the signal amplitude and T_2 relaxation time in sample S1 over a 21-day period after the short-term sedimentation revealed a high degree of stability in both parameters, with only minor fluctuations observed throughout the experiment (see Fig. 11B and E). During this extended monitoring phase, the echo amplitude stayed around 7.0 and the T_2 relaxation time around 2.2 ms (Fig. 11B and E). These findings suggest that, following the initial short-term sedimentation phase, the system approached a state of equilibrium, in which further compaction and internal water redistribution were minimal. The signal amplitude and T_2 relaxation time plots support the conclusion that the most significant changes in the water content and particle settling occurred within the first hour of sedimentation, as captured in the short-term experiment. The extended observation period thus confirmed the absence of any notable long-term sediment densification or water redistribution. This long-term stability in the NMR data is further proved by monitoring the thickness of the sediment layer, which showed no noticeable changes over the 3-week monitoring period. Together, these results confirm stationary conditions in tailings materials subjected to prolonged sedimentation.

4.3. Induced sedimentation (sample S1)

After the long-term monitoring of the sample, additional experiments were conducted to evaluate the impact of gentle mechanical shaking on the NMR signal amplitude and T_2 relaxation time. This phase of the study aimed to assess whether slight mechanical disturbances could promote further compaction of the sediment layer by inducing particle rearrangement and facilitating additional water expulsion from the sedimented tailings porous matrix.

To assess this, sample S1 was subjected to repeated 1-min events of gentle manual shaking over the total period of two hours. NMR measurements were recorded between the shaking events until the end of the induced sedimentation period where no further changes in the NMR signal amplitude and T_2 relaxation time were observed. As a result of this intervention, a notable decrease in signal amplitude was observed from 7.0 to 5.5 (see Fig. 11C). Simultaneously, T_2 relaxation times decreased significantly from 2.2 to 1.3 ms, indicating the
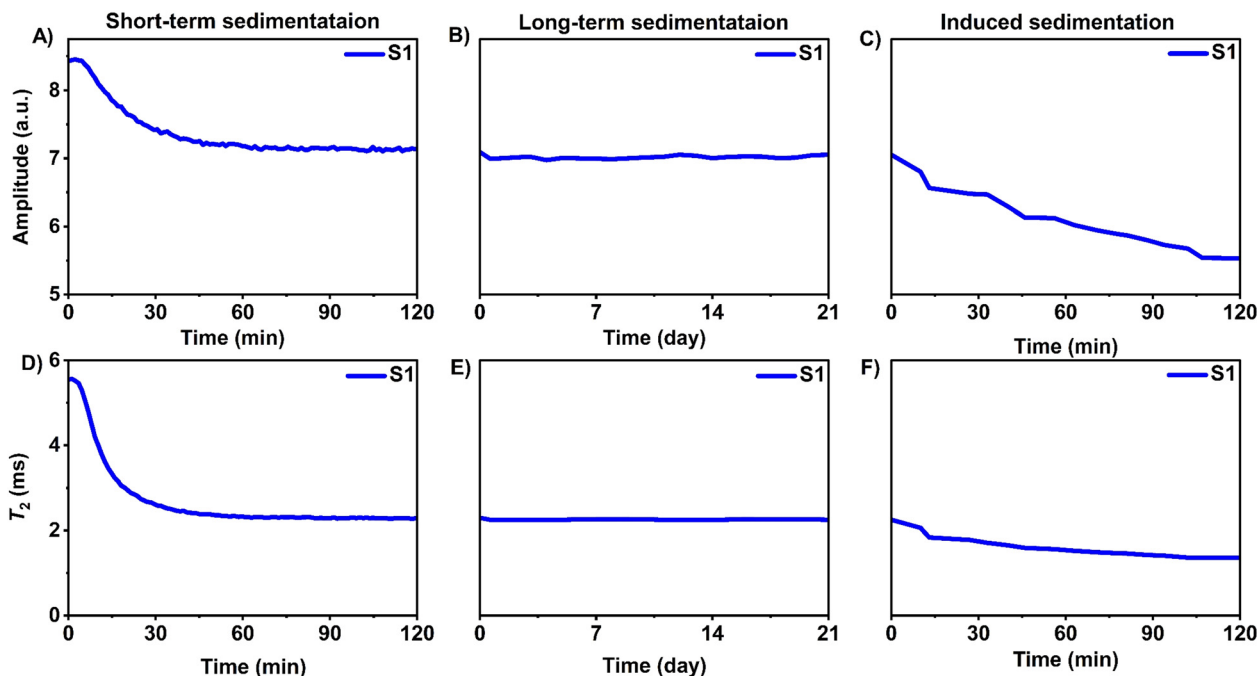
Fig. 11 NMR data across different experiment phases for sample S1. The changes in the signal amplitudes and T_2 relaxation times during the initial 120 minutes of short-term sedimentation are displayed in (A) and (D), respectively, highlighting their rapid changes, followed by stabilization. The long-term stability of these parameters over 21 days is illustrated in (B) and (E), respectively, suggesting insignificant changes and indicating the formation of a metastable sediment layer. The effects of induced sedimentation through mechanical shaking are illustrated in (C) and (F). In this case, a continuous decrease in the NMR signal amplitude and the T_2 relaxation time is observed over the period of 120 minutes, suggesting alterations in sediment compactness and water dynamics.

formation of a more compact and structurally dense sediment layer (Fig. 11F). Monitoring the sediment layer thickness confirmed a compaction of approximately 1.5 mm, aligning with the trends observed in the NMR data. The concurrent reductions in both the echo amplitude and T_2 relaxation time highlight the capability of NMR instrumentation to capture minor yet significant variations in sediment compaction and internal water mobility.

4.4. Sedimentation pattern analysis: influence of physical and mineralogical properties (samples S1–S6)

To investigate the sedimentation behavior of different slurry samples, the NMR-MOUSE instrument was employed to monitor changes in the signal amplitudes and transverse relaxation times (T_2) during a short-term sedimentation experiment lasting 120 min for six distinct samples, S1–S6, collected in various locations of the same TSF.

The analysis revealed distinct variations in both the NMR signal amplitude decrease and T_2 relaxation patterns across the different samples, reflecting differences in settling dynamics (Fig. 12 and 13). The settling behavior of the samples was ranked based on the rate of the NMR signal and T_2 decays, with the following sedimentation order determined: S5 > S2 > S6 > S3 > S4 > S1. Specifically, sample S5 showed the fastest signal amplitude drop with the smallest T_2 decrease (*ca.* 2.6 ms), indicating a rapid transition from suspended to settled state. In contrast, sample S1 exhibited a slow and gradual

signal decay, suggesting prolonged particle suspension and a relatively slow compaction.

To evaluate these observations in further detail, we examined the particle-size distribution data (Fig. 4). These data indicate that samples S5, S2, and S6, which settled more rapidly, shared a key feature of relatively large mean particle diameters (29 to 31 μm). Notably, they also exhibited a bimodal particle size distribution. In particular, S5 had a prominent coarse fraction centered around 55 μm. Apparently, these particles significantly contributed to the observed higher particle settling velocity, as the simple theory described in Section 3.1 implies. A similar trend associated with the presence of big particles was observed in the NMR experiments for the other two samples (S2 and S6). Likewise, a rapid signal drop was detected in the initial moments of the short-term sedimentation, with the signal amplitudes reaching the final plateau between 5 and 15 minutes. In contrast, sample S1 displayed the finest mean particle size (8.95 μm), which facilitated particles being suspended longer due to the reduced settling velocity. This sample exhibited the slowest sedimentation rate among the samples tested, as indicated by the reduction of the echo amplitude from 8.4 to 7.1 arbitrary units over the 50-min period. Clearly, these observations are in qualitative alignment with the classical sedimentation theory, where the settling rate is directly influenced by the particle size, particularly under low-Reynolds-number conditions governed by Stokes' law (Section 3.1).
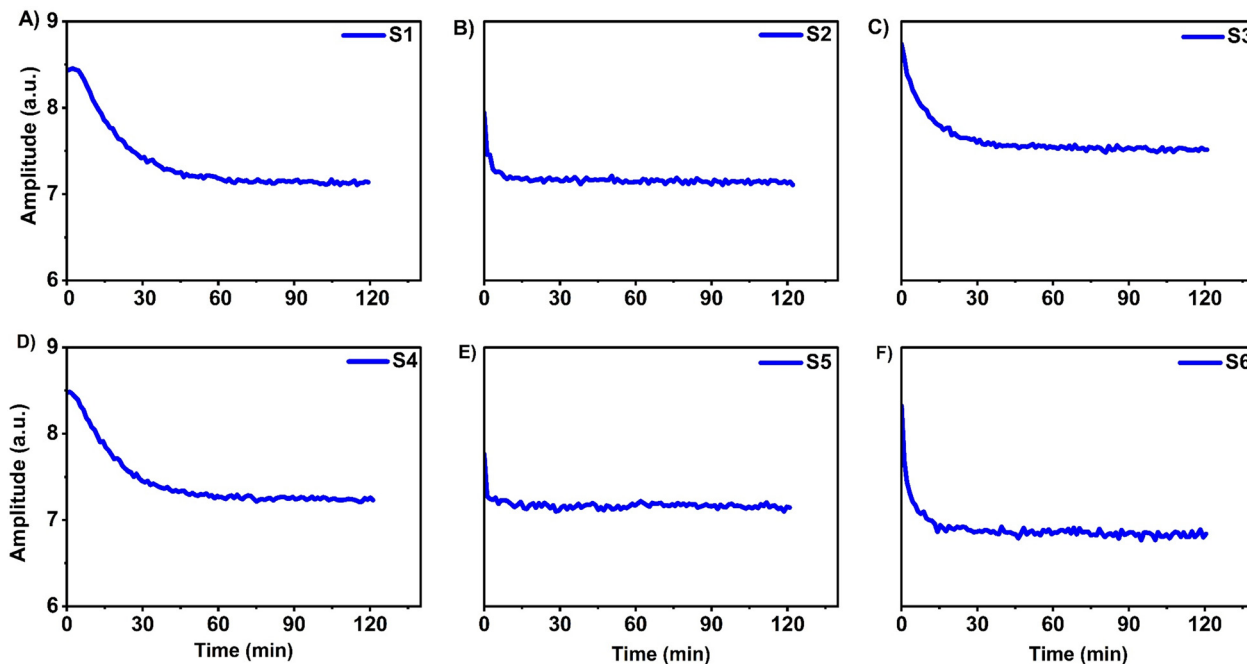
Fig. 12 Experimental ^{1}H NMR signal amplitudes measured during the short-term sedimentation experiments as a function of time (A)–(F) for the samples from S1 to S6, respectively. All curves demonstrated an initial rapid decrease, followed by stabilization in echo amplitude across different samples.
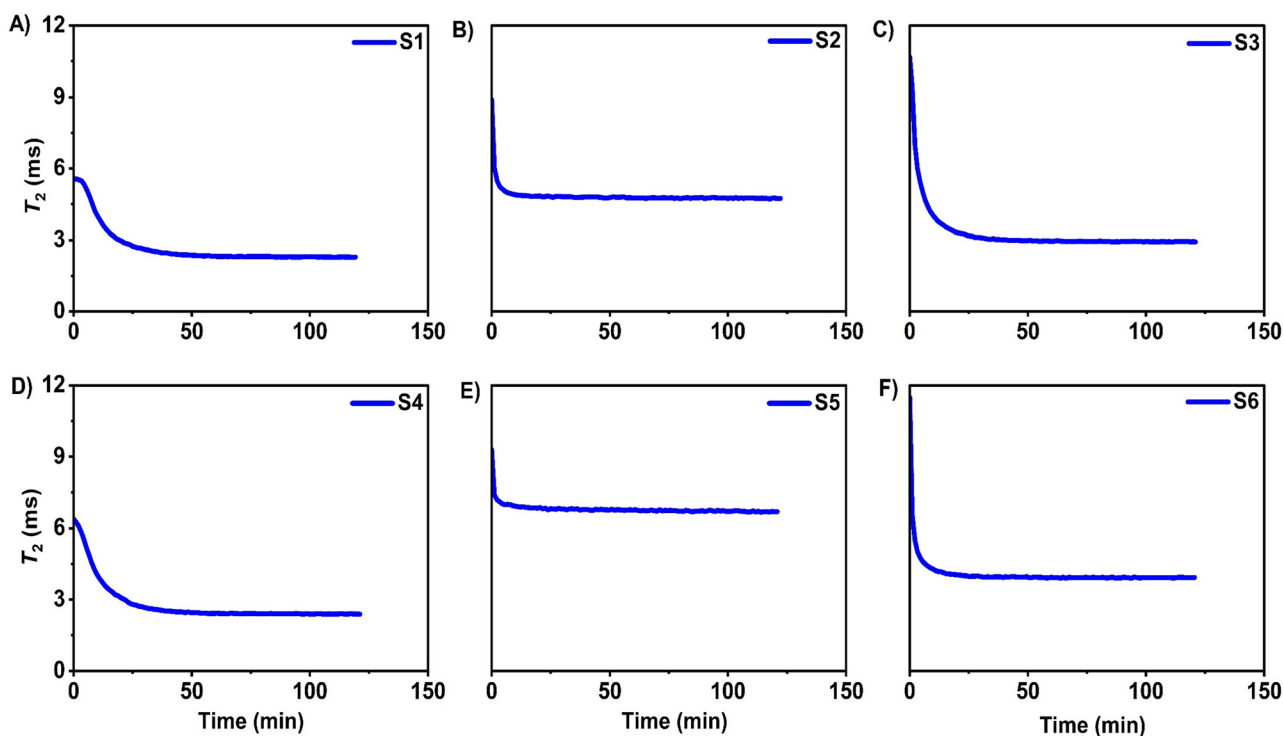

Fig. 13 T_2 relaxation times measured during short-term sedimentation experiments (A)–(F) for samples S1 to S6, respectively. The displayed curves illustrate decreasing T_2 relaxation times, which indicate a transition from free to more confined water states within the sediment.

A comparison between the predictions of Stokes' law, eqn (8), and the experimentally determined values from NMR experiments shows that the measured settling times fall within the theoretical range predicted using available particle size and mineral distribution data for our samples (see Fig. 8 and Section S2.5 in SI). At the same time, the predicted settling

time ranges are broad, illustrating the importance of experimental validations, wherein NMR can serve as a valuable tool. Furthermore, the final T_2 relaxation times measured at the end of the experiments showed that samples S1, S3, and S4, with smaller particle sizes, consistently exhibited lower final T_2 values, indicating more restricted water mobility due to a higher surface-to-volume ratio. In contrast, samples S2, S5, and S6 with larger particle sizes exhibited higher final T_2 relaxation times. Notably, sample S1, which has the slowest sedimentation and finest mean particle size, recorded the lowest final T_2 (*ca.* 2.3 ms), while S5, the fastest-settling sample with a prominent coarse fraction, exhibited the highest final T_2 relaxation time (*ca.* 6.7 ms). These findings demonstrate a strong correlation between the sedimentation rate, particle size, S/V ratio, and water mobility, as captured by low-field NMR.

We also believe that another important factor that may influence the sedimentation process is the solid content percentage. According to the NMR measurements, samples S5, S2, and S6 demonstrated the fastest sedimentation rate and had relatively high solid contents (27.9–29.5%). In contrast, samples S1, S3, and S4, settling more slowly, were characterized by lower solid contents (25.2–26.4%).

In addition, XRD analysis was conducted to assess the influence of mineralogical composition on the settling properties of the tailings samples (Fig. 5). This analysis identified the dominant mineral phases across the samples, including muscovite (mica), gypsum, feldspars (albite and anorthite), quartz, hydronium jarosite, and rutile (see SI Section S2.3 for further details). These phases exhibit a range of densities, from gypsum (2.30–2.37 g cm^{-3})[58] to rutile (4.23–5.50 g cm^{-3}).[58] Importantly, the physical characteristics and morphology of these minerals may also influence the sedimentation behavior beyond density alone. The platy structure of mica,[58] for instance, may reduce the sedimentation efficiency unless counteracted by aggregation or coarse particle formation. In contrast, dense but finely divided phases, such as hydronium jarosite (3.01 g cm^{-3}),[58] are expected to retard the sedimentation.

To evaluate particle sizes associated with specific minerals, a composition elemental analysis was conducted *via* EDS for S1 and S5 (Fig. 6), the samples with the slowest and fastest settling rates, respectively. EDS showed that in S1 and S5, coarser particles were consistently associated with gypsum and muscovite, while albite, quartz, and rutile were typically medium-sized. Hydronium jarosite appeared as the finest-grained component, and its presence was correlated with a delayed settling according to the NMR data.

In sample S1, the high proportion of fine-grained minerals, particularly hydronium jarosite (18%), can contribute to delayed sedimentation. Despite its relatively high density (3.01 g cm^{-3}),[58] EDS analysis revealed that hydronium jarosite was the finest-grained component in sample S1, which may reduce its settling rate, as also supported by the fine PSD and indicated by the gradual decrease in NMR signal.

Conversely, sample S5 showed the fastest sedimentation rate, reaching the NMR signal amplitude plateau within 5 minutes. This can be rationalized through the presence of large particles in the PSD for this sample and the low percentage of fine minerals, which was also proved by the EDS and PSD results. Mineralogically, S5 contained the lowest mica content (10%), minimizing the presence of platy, slow-settling particles. In contrast, it contained 6% of rutile, a dense mineral (4.23–5.50 g cm^{-3}),[58] which has the highest concentration among all samples. Additionally, this sample was dominated by moderately dense minerals, including 30% feldspar (albite and anorthite, 2.62–2.76 g cm^{-3})[58] and 20% quartz (2.65 g cm^{-3}). This combination of large, dense particles and a low amount of flat minerals can contribute to the S5 rapid sedimentation rate.

Moreover, sample S2, which also settled rapidly, contained 16% mica, which would be expected to hinder settling, but this effect was likely mitigated by the large particle sizes, moderate (12%) feldspar (2.62–2.76 g cm^{-3})[58] content and 25% of quartz (2.65 g cm^{-3}).[58] The sample also contained 5% of high-density mineral known as luogufengite (4.905 g cm^{-3})[59] that was defined as others in Fig. 5. Additionally, the presence of 4% rutile (4.23–5.50 g cm^{-3})[58] and 5% hydronium jarosite (3.01 g cm^{-3})[58] may further enhance the sedimentation. This mineralogical composition, combined with large mean particle sizes, the highest solid content, and an abundance of moderate to high-density minerals, contributed to the rapid decay in the signal amplitude from 7.9 to 7.1 units in 9 minutes. This was also visible as a pronounced decrease in the T_2 relaxation time.

Sample S6, despite containing a high proportion of mica (40%), a platy mineral,[58] exhibited relatively rapid settling. This behavior can be attributed to its large mean particle size (30.98 μm), as well as the presence of a moderate amount of feldspar (23%) and 12% of quartz. The observed T_2 relaxation time reduction (from 11.5 to 3.9 ms) and rapid signal stabilization within 15 minutes indicate structural reorganization and progressive dewatering during the sedimentation. These findings suggest that, while platy minerals like mica may hinder settling, their effect can be mitigated when the overall particle size distribution and mineral density are conducive to sedimentation.

Sample S3 showed moderate sedimentation behavior, which was aligned with both its intermediate mica content (26%) and relatively fine mean particle size (10.31 μm). It also included 7% jarosite and 3% rutile, which could improve the settling if these minerals had been coarser. However, this sample was dominated by platy and low-density minerals, while the high-density components were likely too fine to significantly influence settling. Accordingly, a moderate sedimentation rate was observed, reflecting the balance between opposing sedimentation influences.

Sample S4, with a mean particle size of 16.72 μm and a solid content of 26.1%, reached a stable signal amplitude over about 50 minutes, indicating a gradual sediment compaction process. This sample contained 30% mica, a significant proportion of platy minerals that may inherently resist settling. Although S4 contained 3% rutile and 6% jarosite, these dense minerals were likely to be too fine to improve settling.

Samples S3 and S4 exhibited the highest initial and final signal amplitudes. S3 also showed the highest initial T_2 relaxation time

(10.67 ms) in the short-term sedimentation experiment. This behavior can be attributed to their low solid contents (S3 = 25.2%, S4 = 26.1%) and the highest combined content of mica and gypsum among all samples, as these minerals have shown the ability to retain water in their structures.[56,60,61]

These findings underscore that while particle size is the primary driver of sedimentation dynamics, mineral composition and density further modulate the settling behavior. Coarse high-density minerals tend to promote rapid sedimentation when present in sufficient amounts. In contrast, even high-density phases, such as hydronium jarosite, can impede settling when finely dispersed, due to their high surface area and tendency to remain suspended.

4.5. Induced sedimentation experiment for S3–S6

Following the observation of notable compaction and changes in NMR signal behavior in sample S1 under induced sedimentation, a subsequent set of measurements was carried out for samples S3–S6 to determine whether similar processes would occur in samples with varying mineralogical and physical characteristics. In these experiments, all samples were subjected to gentle shaking over a 2-hour period (see Section 2.3.3 for details), with real-time monitoring conducted using the NMR-MOUSE system. Under the gentle shaking conditions, all tested samples exhibited a consistent response profile, characterized by a measurable decrease in the echo amplitude and transverse relaxation time (Fig. 14), in agreement with the behavior described for S1 in Section 4.3.

This trend indicates enhanced sediment compaction and decreased water mobility within the sediment layer. The drop in echo amplitude reflects the increased particle packing, while the T_2 reduction signifies a transition from free to more confined water states. Reaching the final plateau points, where the gentle shaking events do not result in any further changes in the signal amplitude and T_2 relaxation time, indicates that induced sedimentation drives the sediment structure toward a genuinely stable state, in contrast to the metastable one established after the short-term sedimentation experiment.

The uniformity of the responses across samples suggests that the low-intensity mechanical input can promote additional compaction of the tailings sediments regardless of their mineralogical differences.

4.6. Drying experiment (sample S1)

Following the completion of sedimentation experiments, sample S1 was subjected to a controlled drying protocol. After the removal of the supernatant water, the remaining sediment was exposed to a continuous flow of compressed air at a rate of 1 cubic foot per hour (cfh) (ca. 472 cm^3 min^{-1}). During this phase, NMR was employed to monitor changes in signal amplitudes and transverse relaxation times (T_2) at three discrete sludge depths: 0.7 (bottom), 1.7 (middle), and 2.7 mm (top), Fig. 3. This depth-resolved approach enabled spatial tracking of drying kinetics and moisture redistribution within the sediment layer.

As shown in Fig. 15, the echo amplitude decreased progressively over time at all monitored depths. The surface layer (2.7 mm) exhibited the highest initial signal, attributed to the residual water retained after supernatant removal, and it showed the most rapid decline in amplitude, consistent with enhanced evaporation near the air-exposed interface. In contrast, the deep layers displayed a relatively slow rate of signal loss. Nevertheless, the signal amplitude at all depths eventually
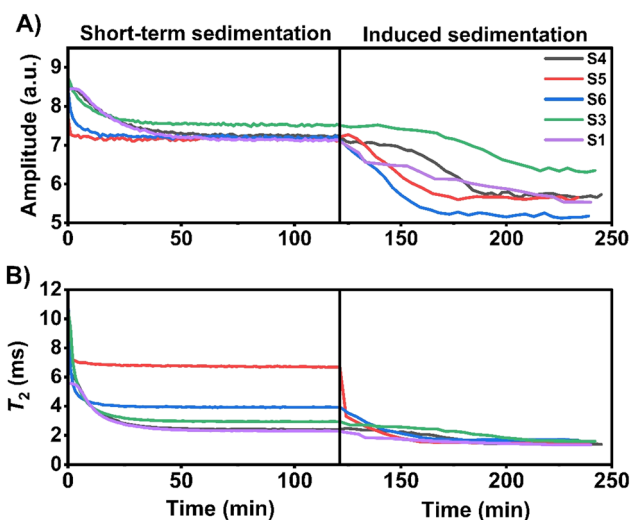

Fig. 14 Comparative analysis of echo amplitudes (A) and T_2 relaxation times (B) for samples S1 and S3–S6 during the short-term sedimentation and subsequent gentle shaking. The left panels show the initial sedimentation phase, highlighting rapid changes in both parameters, while the right panels illustrate the impact of mechanical shaking, marked by further reductions in amplitude and T_2 relaxation, indicating enhanced sediment compaction and water confinement.
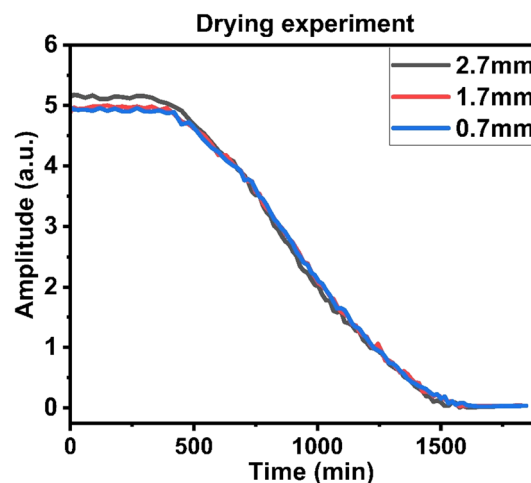

Fig. 15 Drying kinetics for sample S1 exposed to a continuous flow of compressed air at a rate of 1 cubic foot per hour. The monitoring was done through signal amplitude measurements at three depths (0.7, 1.7 and 2.7 mm; see Fig. 3). The plot tracks the amplitude reduction to zero across all depths, indicating moisture expulsion from the sediment during the drying experiment.
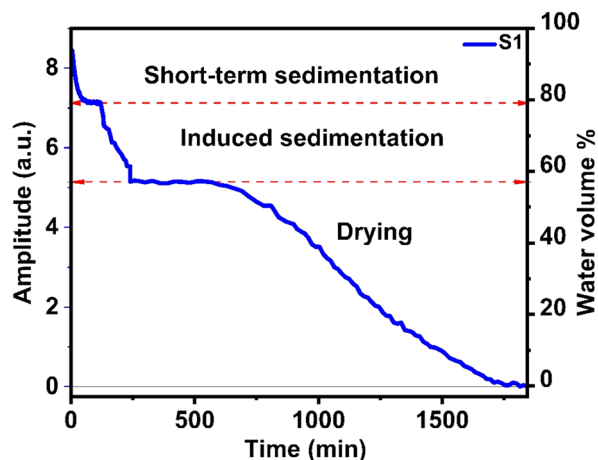
Fig. 16 Sequential changes in the NMR signal amplitude and water-volume percentage for sample S1 across different treatment stages: short-term sedimentation, induced sedimentation, and drying. This plot shows the reduction in the signal amplitude, which corresponds to the changes in the water content from the beginning of sedimentation to the end of the drying process. Key phases are indicated to highlight significant transitions in the sediment's characteristics.

decreased to zero, confirming full moisture removal throughout the vertical profile of the sediment.

Similarly, the evolution of the T_2 relaxation times of water during the drying experiment showed a systematic decrease from 1.2 to 0.6 ms, consistent with the reduction of water mobility (Fig. S52 and S53 of SI). At the final stages of this experiment, however, due to the significant water loss, the signal-to-noise ratio became too low to perform quantitative T_2 analysis. The corresponding T_2 data and detailed descriptions are provided in Section S2.7 of SI.

To provide a comprehensive view of the moisture behavior during the experimental sequence, Fig. 16 illustrates changes in the signal amplitudes for sample S1 from initial sedimentation through to the final drying stage. The first 50 minutes were marked by a sharp amplitude reduction, corresponding to the rapid formation of a sediment layer and the depletion of free water from the NMR-sensitive region. This behavior aligns with visual observations of particle settling and stratification within the container.

Following the short-term sedimentation phase, long-term sedimentation for three weeks was conducted. However, due to the negligible changes in the signal amplitude, the data were excluded from the plot to emphasize the dynamic transitions. Subsequent induced sedimentation, achieved *via* gentle shaking, resulted in a further decrease in the NMR signal amplitude. This was observed after the initial short-term sedimentation plateau, indicating further water redistribution and the compaction of the sediment layer during the induced sedimentation.

In the final phase, the drying procedure was initiated. After the mechanical removal of residual supernatant water, the sample was subjected to airflow drying. The signal amplitude steadily decreased to zero, indicating full dehydration of the sediment, as detected by the NMR.

In addition, Fig. 16 shows the water volume percentage as a function of time during the experiment (right vertical scale), giving an overall picture of moisture dynamics from the start of sedimentation to drying. To determine this parameter, the signal amplitude was compared to our standard 100% water sample (0.1 M $CuCl_2 \cdot 2H_2O$ solution in the same size container). At the beginning of the short-term sedimentation, when the sediment layer had not yet been formed within the sensitive measuring volume (Fig. 3A), the signal amplitude was 94% relative to that of the standard sample, indicating a high initial water content that gradually decreased to zero at the end of the drying process. This offers a thorough quantitative analysis of the water dynamics throughout the experiment, highlighting the transition from loosely bound water to increasingly confined states within the tailings matrix. The reliability of the measured water content obtained based on the NMR signal amplitudes at the final stage of the drying experiment was checked using gravimetrical analysis. For this purpose, after the completion of the NMR air-drying experiment, the remaining sediment sample was weighed and placed in an oven for 4 h at 105 °C. The weight difference before and after oven-drying was found to be 3.4% of the total water initially present in the sediment before the air-drying (see Section S2.6 in SI). Comparison of these results confirms that more than 96% of the total mobile water content was detected by NMR with the given NMR signal-to-noise ratio and experimental parameters.

5. Conclusion

This study demonstrated the capability of low-field, single-sided NMR to effectively monitor sedimentation and drying processes in complex tailings materials from a gold mining facility. Through a real-time measurement of the ^{1}H NMR signal amplitude and T_2 relaxation times, it was possible to capture detailed moisture dynamics, track sediment-layer formation, and assess the progression of dewatering across distinct experimental conditions.

The short-term sedimentation experiments revealed significant variability in settling behavior across six tailings samples (S1–S6), which was primarily governed by the particle-size distribution and further modulated by mineralogical composition and solid content. Samples characterized by larger mean particle sizes and higher proportions of dense minerals (*e.g.*, quartz, anorthite, and illite) exhibited more rapid settling, as evidenced by faster signal decrease and longer final T_2 relaxation times. In contrast, samples with finer particle sizes, particularly those enriched in hydronium jarosite, showed delayed settling and slower compaction kinetics.

Long-term sedimentation experiments confirmed that most structural changes within the sediment layer occurred within the first hour, with minimal compaction or water redistribution observed thereafter. Induced sedimentation achieved through gentle mechanical shaking led to further signal decay and T_2 reduction, indicating enhanced sediment compaction and water expulsion not achievable under static conditions. These

findings underscore the importance of the external energy input in accelerating sedimentation in tailings materials.

The controlled drying experiment further highlighted the efficiency of single-sided NMR in capturing depth-resolved moisture dynamics. The progressive decrease in signal amplitude across multiple sludge depths, culminating in a complete signal loss, demonstrated the sensitivity of this method in tracking drying fronts and total moisture loss. Quantitative calibration against a standard water sample enabled the estimation of water-volume changes throughout the sedimentation and drying sequence.

Overall, this work establishes low-field single-sided NMR as an analytical tool for evaluating sedimentation, induced compaction, and drying behavior in heterogeneous mining tailings. By integrating NMR measurements with particle size and mineralogical data, the study provides a comprehensive framework for assessing how physical and compositional properties influence dewatering efficiency.

Author contributions

This work was done through the following contributions: S. H. D.: investigation, validation, visualization, writing – original draft; J. N.: supervision (mining site), coordination of sampling logistics, technical guidance on TSF operations, provision of field-specific information, writing – review and editing; M. P.: technical support related to TSF and mining operations, assistance in data collection, writing – review and editing; J. K.: field support with sampling activities at the facility, writing – review and editing; A. A.: project coordination at the mining site, logistical support, access facilitation, writing – review and editing; S. L.: mineralogical consultation, support on mining-related scientific context, writing – review and editing; P. S.: consultation, assistance with mineralogical characterization and PSD analysis, writing – review and editing; V.-V. T.: funding acquisition, resources, supervision, validation, writing – review and editing; E. K.: conceptualization, funding acquisition, supervision, validation, writing – review and editing; V. V. Z.: conceptualization, funding acquisition, resources, supervision, investigation, validation, visualization, writing – review and editing.

Conflicts of interest

There are no conflicts to declare.

Data availability

The raw data for this article are available at fairdata.fi at https://doi.org/10.23729/fd-351a0ff2-97ab-33da-88da-9a773cf80994.

The data supporting this article have been included as part of supplementary information (SI). The following supplementary information is available: detailed description of materials and methods; sample preparation procedures; description of fitting model for T_2 relaxation time calculations; repeatability tests of short-term sedimentation; detailed results of PSD, XRD, and SEM-EDS analyses; calculations of theoretical settling characteristics using Stokes' law; estimation of internal magnetic field gradients and their effect on T_2 decays; determination of accuracy of water content and T_2 relaxation times in drying experiments. See DOI: https://doi.org/10.1039/d5cp03347k.

References

1 F. P. Carvalho, *Food Energy Secur.*, 2017, **6**, 61–77.
2 E. Schoenberger, *Resour. Policy*, 2016, **49**, 119–128.
3 R. Obenaus-Emler, M. Falah and M. Illikainen, *Constr. Build. Mater.*, 2020, **246**, 118470.
4 M. G. Lemos, T. Valente, A. P. Marinho-Reis, R. Fonsceca, J. M. Dumont, G. M. M. Ferreira and I. D. Delbem, *Mine Water Environ.*, 2021, **40**, 257–269.
5 A. H. Hesketh, J. L. Broadhurst and S. T. L. Harrison, *Miner. Eng.*, 2010, **23**, 225–229.
6 E. Furnell, K. Bilaniuk, M. Goldbaum, M. Shoaib, O. Wani, X. Tian, Z. Chen, D. Boucher and E. R. Bobicki, *ACS ES&T Eng.*, 2022, **2**, 728–745.
7 C. Wang, D. Harbottle, Q. Liu and Z. Xu, *Miner. Eng.*, 2014, **58**, 113–131.
8 F. A. M. Marinho, Y. Corrêa, R. Soares, I. D. Carvalho and J. P. de Sousa Silva, *Geosciences*, 2024, **14**, 273.
9 X. Ji, Q. Xu, K. Ren, L. Wei and W. Wang, *Water*, 2024, **16**, 2958.
10 Z. Lyu, J. Chai, Z. Xu, Y. Qin and J. Cao, *Adv. Civ. Eng. Mater.*, 2019, **2019**, 1–18.
11 M. Rico, G. Benito, A. R. Salgueiro, A. Díez-Herrero and H. G. Pereira, *J. Hazard. Mater.*, 2008, **152**, 846–852.
12 S. Jeeravipoolvarn, R. J. Chalaturnyk and J. D. Scott, *Comput. Geotech.*, 2009, **36**, 751–761.
13 H. M. Shodja and J. R. Feldkamp, *Int. J. Numer. Anal. Methods Geomech.*, 1993, **17**, 753–769.
14 V. Pane and R. L. Schiffman, *Geotechnique*, 1985, **35**, 69–72.
15 E. A. Toorman, *Geotechnique*, 1999, **49**, 709–726.
16 W. F. Eckert, J. H. Masliyah, M. R. Gray and P. M. Fedorak, *AIChE J.*, 1996, **42**, 960–972.
17 M. D. Bonin, A. R. Cabral and M. Nuth, *Geotech. Test. J.*, 2019, **42**, 1493–1517.

18 W. Zhang, C. Zhang, X. Lei, S. Quintero Olaya, Y. Zhu, Z. Zhao, S. Jensen and D. J. Williams, *Acta Geotech.*, 2024, **19**, 1891–1909.

19 J. Bian, H. Wang, C. Xiao and D. Zhang, *PLoS One*, 2018, **13**, e0204230.

20 Y. Li and D. van Zyl, *Miner. Eng.*, 2024, **208**, 108580.

21 B. Blümich, *Essential NMR: For Scientists and Engineers*, Springer, Cham, 2019.

22 J. Keeler, *Understanding NMR spectroscopy*, John Wiley & Sons, Chichester, 2nd edn, 2010.

23 A. Abragam and H. Y. Carr, *Phys. Today*, 1961, **14**, 56–58.

24 S. C. M. Cabrera, J. Bryan, B. Komishke and A. Kantzas, *Int. J. Min., Reclam. Environ.*, 2009, **23**, 33–50.

25 B. Blümich, F. Casanova, J. Perlo, F. Presciutti, C. Anselmi and B. Doherty, *Acc. Chem. Res.*, 2010, **43**, 761–770.

26 E. Del Federico, S. A. Centeno, C. Kehlet, P. Currier, D. Stockman and A. Jerschow, *Anal. Bioanal. Chem.*, 2010, **396**, 213–220.

27 L. Brizi, V. Bortolotti, G. Marmotti and M. Camaiti, *Magn. Reson. Chem.*, 2020, **58**, 889–901.

28 B. Blümich, J. Perlo and F. Casanova, *Prog. Nucl. Magn. Reson. Spectrosc.*, 2008, **52**, 197–269.

29 S. Meiboom and D. Gill, *Rev. Sci. Instrum.*, 1958, **29**, 688–691.

30 V. Stagno, S. Mailhiot, S. Capuani, G. Galotta and V.-V. Telkki, *J. Cult. Herit.*, 2021, **50**, 95–105.

31 A. Guthausen, G. Guthausen, A. Kamlowski, H. Todt, W. Burk and D. Schmalbein, *J. Am. Oil Chem. Soc.*, 2004, **81**, 727–731.

32 Y. Kharbanda, S. Mailhiot, O. Mankinen, M. Urbańczyk and V.-V. Telkki, *J. Dairy Sci.*, 2023, **106**, 1586–1595.

33 M. C. Tourell, T. S. Ali, H. J. Hugo, C. Pyke, S. Yang, T. Lloyd, E. W. Thompson and K. I. Momot, *Magn. Reson. Med.*, 2018, **80**, 1243–1251.

34 T. S. Ali, M. C. Tourell, H. J. Hugo, C. Pyke, S. Yang, T. Lloyd, E. W. Thompson and K. I. Momot, *Magn. Reson. Med.*, 2019, **82**, 1199–1213.

35 X. Huang, T. S. Ali, T. Nano, T. Blick, B. W.-C. Tse, K. Sokolowski, M. C. Tourell, T. Lloyd, E. W. Thompson, K. I. Momot and H. J. Hugo, *Magn. Reson. Imaging*, 2019, **62**, 111–120.

36 E. Rössler, C. Mattea, S. Saarakkala, P. Lehenkari, M. Finnilä, L. Rieppo, S. Karhula, M. T. Nieminen and S. Stapf, *NMR Biomed.*, 2017, **30**, e3738.

37 Y. Kharbanda, M. Urbańczyk, V. V. Zhivonitko, S. Mailhiot, M. I. Kettunen and V. V. Telkki, *Angew. Chem., Int. Ed.*, 2022, **61**, e202203957.

38 N. H. Williamson, R. Ravin, T. X. Cai, M. Falgairolle, M. J. O'Donovan and P. J. Basser, *PNAS Nexus*, 2023, **2**, pgad056.

39 J. Li, S. Mailhiot, A. M. Kantola, H. Niu, H. Sreenivasan, V.-V. Telkki and P. Kinnunen, *Cem. Concr. Res.*, 2022, **160**, 106921.

40 T. Colinart and P. Glouannec, *Energy Procedia*, 2015, **78**, 1484–1489.

41 R. S. Holthausen, C. Glawe, J. Sieksmeier and M. Raupach, *ce/papers*, 2023, **6**, 1673–1679.

42 M. I. Velasco, E. V. Silletta, C. G. Gomez, M. C. Strumia, S. Stapf, G. A. Monti, C. Mattea and R. H. Acosta, *Langmuir*, 2016, **32**, 2067–2074.

43 S. Yao, C. Chang, K. Hai, H. Huang and H. Li, *J. Pet. Sci. Eng.*, 2022, **208**, 109211.

44 L. Raffaele, L. Bruno and D. J. Sherman, *Aeolian Res.*, 2020, **44**, 100593.

45 J. Dueck, *Adv. Powder Technol.*, 2013, **24**, 150–153.

46 W. E. Dietrich, *Water Resour. Res.*, 1982, **18**, 1615–1626.

47 Y. S. Chong, D. A. Ratkowsky and N. Epstein, *Powder Technol.*, 1979, **23**, 55–66.

48 T. E. Baldock, M. R. Tomkins, P. Nielsen and M. G. Hughes, *Coastal Eng.*, 2004, **51**, 91–100.

49 P. J. T. Dankers and J. C. Winterwerp, *Cont. Shelf Res.*, 2007, **27**, 1893–1907.

50 D. Pal and K. Ghoshal, *Adv. Water Resour.*, 2013, **60**, 178–187.

51 J. H. Baas, M. L. Baker, P. Buffon, L. J. Strachan, H. C. Bostock, D. Hodgson, J. T. Eggenhuisen and Y. T. Spychala, *Depositional Rec.*, 2022, **8**, 603–615.

52 J. Kowalewski and L. Mäler, *Nuclear Spin Relaxation in Liquids: Theory, Experiments, and Applications*, CRC Press, Boca Raton, 2nd edn, 2017.

53 B. Blümich, S. Anferova, R. Pechnig, H. Pape, J. Arnold and C. Clauser, *J. Geophys. Eng.*, 2004, **1**, 177–180.

54 *Advanced Characterization Techniques, Diagnostic Tools and Evaluation Methods in Heritage Science*, ed. D. M. Bastidas and E. Cano, Springer, Cham, 2018.

55 K. R. Brownstein and C. E. Tarr, *Phys. Rev. A:At., Mol., Opt. Phys.*, 1979, **19**, 2446–2453.

56 R. L. Kleinberg and M. A. Horsfield, *J. Magn. Reson.*, 1990, **88**, 9–19.

57 R. M. E. Valckenborg, L. Pel and K. Kopinga, *J. Magn. Reson.*, 2001, **151**, 291–297.

58 W. A. Deer, R. A. Howie and J. Zussman, *An Introduction to the Rock-Forming Minerals*, Mineralogical Society of Great Britain and Ireland, London, 3rd edn, 2013.

59 H. Xu, S. Lee and H. Xu, *Am. Mineral.*, 2017, **102**, 711–719.

60 N. O. Ovchinnikov, L. P. Nikitina, M. S. Babushkina, A. K. Yakovleva, Y. N. Yakovlev, O. G. Chernova and S. A. T. Redfern, *Mineral. Mag.*, 2002, **66**, 491–512.

61 G. H. A. van der Heijden, L. Pel, H. P. Huinink and K. Kopinga, *Chem. Eng. Sci.*, 2011, **66**, 4241–4250.